A new nature of microporous architecture with hierarchical porosity and membrane template via high strain rate collision

Rija Nirina Raoelison, Jishuai Li, Thaneshan Sapanathan, Essole Padayodi, Nicolas Buiron, Dany Racine, Zhan Zhang, Daniel Marceau, Mohamed Rachik

A new nature of microporous architecture with hierarchical porosity and membrane template via high strain rate collision

Rija Nirina Raoelison[1,2*], Jishuai Li[1], Thaneshan Sapanathan[1,3], Essole Padayodi[4], Nicolas Buiron[1], Dany Racine[5], Zhan Zhang[5], Daniel Marceau[5], Mohamed Rachik[1]

[1] Sorbonne universités, Université de technologie de Compiègne, Laboratoire Roberval, CNRS UMR-7337, Compiègne, France
[2] Université de Bourgogne Franche-Comté - UTBM, Laboratoire Interdisciplinaire Carnot de Bourgogne, UMR 6303 CNRS, 90100 Belfort, France
[3] Institute of Mechanics, Materials and Civil Engineering, UCLouvain, 1348 Louvain-la-Neuve, Belgium
[4] University of Bourgogne Franche-Comté - UTBM, ELLIADD, Pôle ERCOS, 90010 Belfort, France.
[5] CURAL-REGAL, Université du Québec à Chicoutimi, Saguenay, QC, Canada

Corresponding author: Rija Raoelison rija-nirina.raoelison@utbm.fr (+33 384583097)

Abstract

This paper presents the formation of an unusual porous structure at Al/Al interface joined by magnetic pulse welding. The porous structure consists of a hierarchical microporous architecture with pore size of less than 2µm that represents more than 80% over the whole area, in which 38% of them are sub-micron size pores. It also exhibits ultra-thin wall, sufficiently thin enough to behave as an electron-transparent material with a wall thickness of 50nm. The formation of this porous structure is attributed to a cavitation process of a molten material in three stages including, (1) nucleation, (2) growth and coalescence and (3) solidification. Further analysis of this cavitation process using a dedicated numerical simulation reveals that the nucleation and growth of pores may arise from vaporization governed by a rapid isothermal and isochoric expansion of liquid metal due to the high rate of depressurization. This result explains the potential mechanism of coalescence for the creation of the open porosity. The difference between cavitation onset and highly developed porous structure is attributed to the difference in depressurization during various welding conditions. Welding performed with high intense collision enables to have large impact pressure, therefore those welding conditions provide higher depressurization gap and severe fluid rupture due to significantly large inherent surface tension of the fluid. A fast solidification at a high cooling rate of 10 °C/ns enables to freeze the micropores and resulting with the solidified porous architecture.

Key words: porous structure, micro-pores, ballistic collision, cavitation, depressurization

1. Introduction

Porous materials are increasingly become attractive and offer superior functional properties including energy absorption [1], catalytic performances [2], conduction capabilities [3], removal or cleaning functions [4], energy storage capabilities [5] and osteointegration properties [6]. Those functional capabilities of metallic porous structures have been widely exploited, while the growing interest is given to the performance of micron and submicron size porous structures. Microporous materials are particularly attractive to fulfil new technological requirements and their elaboration recently received significantly high interest from the industry and scientific community. The available literatures on the processing methods of such microporous materials support various porous architectures resulting from specific processes.

During the manufacturing processes of porous structures, the required microporosity was obtained using various phenomenological principles. These phenomenological principles can be classified into four generic categories such as (1) powder stacking-consolidation [6], (2) selective removal process [7], (3) template-assisted method and [1,6] (4) in-situ synthesis of porous structure [8,9]. In a powder stacking-consolidation process, the porosities mainly occur during sintering or thermal spraying deposition of micron size powders, while the compaction of the powder is controlled to promote the formation of micropores between the unbonded surfaces (Fig. 1a). This manufacturing method is rather simple and rapid; however, it has a limitation in terms of reaching very high porous density. For instance, considering a lattice of a simple cubic system, the compactness is stable with the maximum of 50%, highlighting the limitation of the powder stacking-consolidation method. A post chemical corrosion treatment is mostly suggested to increase the porosity after the powder stacking-consolidation process. The chemical corrosion treatment is also known as the selective removal method that can be also applied to fully dense metallic structures. A selective chemical dealloying produces the porosity [10,11].. The selective removal methods also use some other dissolution mechanisms such as centrifugation [12] or thermally activated disintegration via laser irradiation or combustion or heat treatment [13–15]. The use of

removal template offers the possibility to obtain a regular porous architecture with a tailored porosity. These capabilities highlight the effectiveness of the selective removal method to produce micro/nano pores with increase in porous density (Fig. 1b). However, this method requires a costly preparation and post-treatment to obtain a clean porous structure. Some other studies suggest a template-assisted method using a solid porous preform produces a primary porous structure, while subsequent adsorption reaction caused by a carbonization process increases the porosity [13]. Furthermore, using a skeleton as the pre-porous structure that can also be coated using a chemical vapour deposition or an electrolytic reaction [1,6], to produce a porous structure composed of a specific material deposit (Fig. 1c and d).

In-situ synthesis of porous structure is based on a cavitation phenomenon. This method is also known by “foaming” and it has been widely considered to produce large pores. Nevertheless, in recent research studies, the cavitation method has also been successfully applied to the synthesis of small pores in micron size. Electrodeposition is another viable method that can generate dynamic hydrogen bubbles while solid phase coalesces from the bubbles wall and grows between the bubbles during an electrolytic reaction (Fig. 1e and f) [8].

However, the increasing demand for the porous materials requires innovative methods to manufacture the porous structure. Recently, it was found that a ballistic collision enables a cavitation phenomenon that can produce a micro/nano-porous metallic structure [16]. Thus, this work focusses to explore the detail of the porous structure formation, at an interface of a high-speed impact (HSI) welded joint. It is identified that HIS process enables to produce high porosity with thin membrane wall pours structure at an Al/Al welded interface. Eulerian numerical simulation considering the thermomechanical phenomena during the process enables to understand the fundamental mechanism of the porous structure formation.

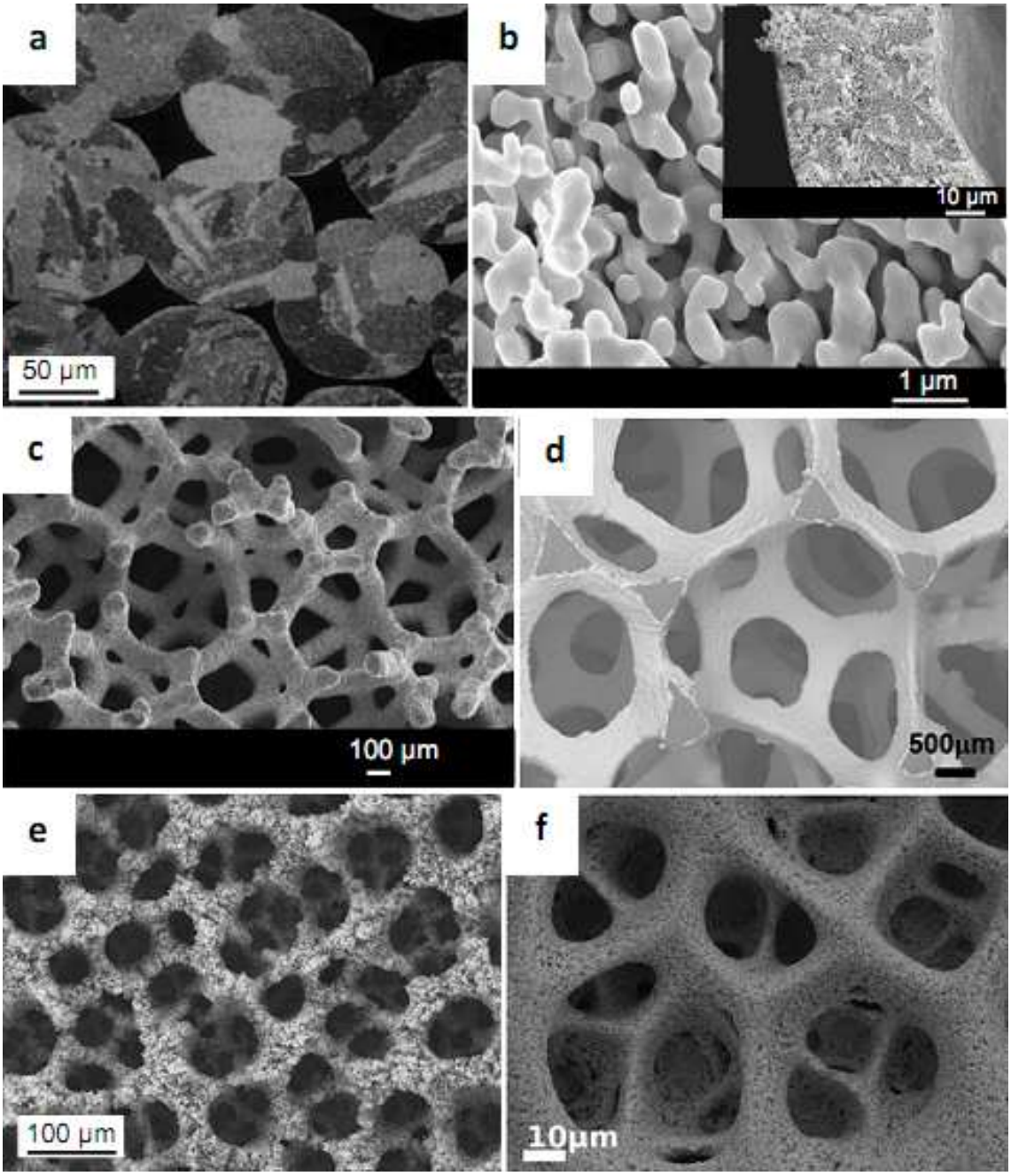

Fig. 1. Typical morphologies of porous structures produced by (a) powder stacking-consolidation [6], (b) selective removal method [7], (c) template-assisted coating using chemical vapour deposition [6], (d) template-assisted coating using electrocatalytic reaction [1] and (e, f) in-situ synthesis of porous structures resulting from hydrogen bubbling assisted electrodeposition [8,9].

2. Porous structure formation using a ballistic collision

Magnetic pulse welding (MPW) is a high-speed impact welding process, had a growing attention over the past four decades and investigated to fabricate welded joints of various material combinations in different geometrical configurations. During an investigation for identifying the appropriate conditions for producing a welded joint using MPW, we made a serendipitous discovery of porous architecture that exhibits a very unusual feature. The porous structure is generated when a hollow tube of aluminium AA6061-T6 impacts on a motionless inner rod of the same material. The high-speed impact is produced by MPW device that induces Lorentz force due to an impulse magnetic field when an electrical discharge of some kV supplied using total capacitance of 690µF, flows through a 3-turn coil combined with a fieldshaper. A Rogowski probe was used to measure the discharge current which has a frequency of 10kHz. Our previous studies [17–19] using various such experimental conditions suggest that the interface is subjected to the ballistic impact and form a bonded joint, but detail analysis of the interface produced under some welding conditions revealed confinement of porous architecture having a singular characteristics, those are investigated in detail in this study.

3. Characteristics of the porous structure

Scanning electron microscopy (SEM) observation of a post-debonded weld surface obtained for an input voltage of 7.5 kV reveals a porous template that consists of hierarchical micro-porous structure formed by spherical pores (Fig. 2). The microstructure reveals a random allocation of the pores and a stochastic porosity. The pores are interconnected like an open cells structure, and are larger than the solid membrane space between them, indicating an apparent high specific surface with a low relative density. Such template conceals the potential of HSI process to generate porous structure with specific characteristics compared to those produced by various processes shown in Fig. 1.

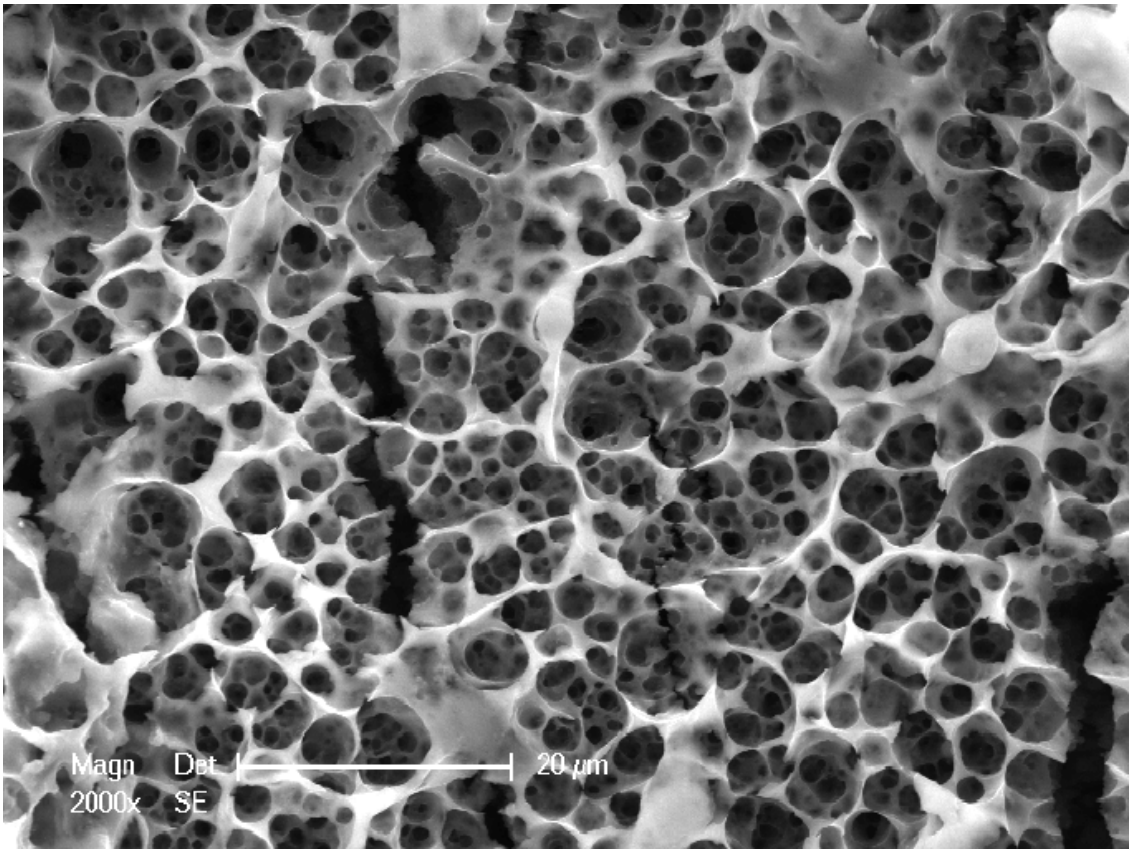

Fig. 2. SEM observation of hierarchical and stochastic open porosity produced by HSI process.

Another SEM observation in Fig.3 reveals the porous media wrapped inside a thin wall membrane structure and additional peculiar details of the porous zone. Fig.3 shows adjacent pores inside the porous media. The pores are organized like a honeycomb structure (Fig. 3) behind a wall. The visualisation of inner pores from outside is possible due to the presence of sufficiently thin outer wall that becomes transparent during the SEM observation. The transparency itself is not an optical property as viewed on (Fig. 3). Rather, this result indicates that the observed transparency is an electron response of the wall under the secondary electron (SE) imaging technique during the SEM observation. Transparency to electrons is widely used in transmission electron microscope (TEM) observation for fine structural characterization. Those TEM samples are generally ultrathin with a thickness of some nm and the analysis is rather focus on the electron transmission across the sample towards an electron detector.

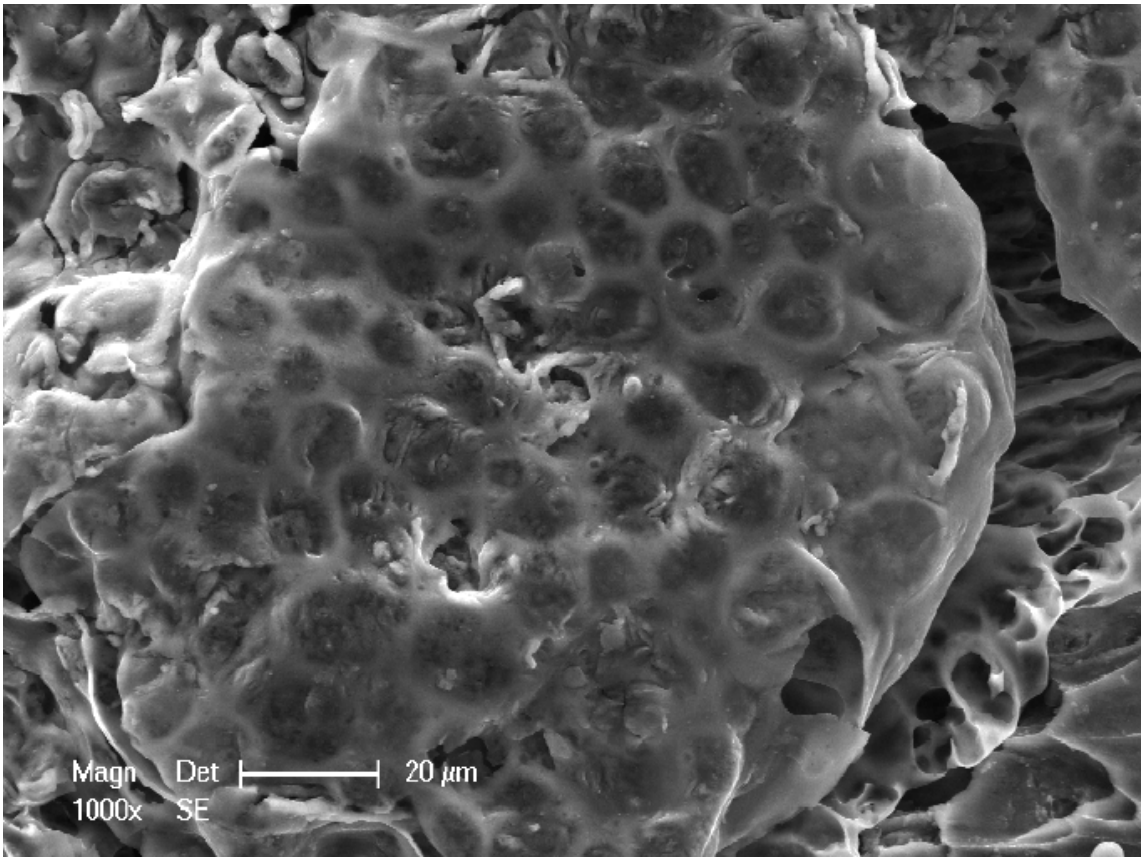

Fig. 3. Typical membrane structure of the porous architecture evidenced through the outer membrane wall.

Recently, the combination of electron transparency analysis with SEM observation has received an attention for electron microscopy observation of liquid samples [20, 21]. A liquid specimen enclosed by an ultrathin membrane, less than 100nm thick, was sufficiently thin to act as an electron transparent material. Thus, a similar fact can explain the transparency of the thin wall membrane during the SEM observation (Fig. 3). That is, the outer wall of the porous template may behave like an electron-transparent material while capturing the topographic details under SE mode. There is a variance in thickness between the outer wall and the thickness of the inner structure which appears like honeycomb structure. The outer encapsulating wall is likely thinner than the honeycomb wall which is roughly about a few µm (Fig. 3). Fig. 4 provides further insight on the thickness of the membrane wall that behaves like an electron-transparent material. The porous walls clearly show the front template and exhibit also back pore cell, i.e. from behind. Such pore cell appears as darker zone that can also be viewed through the membrane wall. This electron-transparent zone is

not thick enough to be measured. Therefore, an image analysis technique was used to determine the thickness of the membrane and identify that the wall has a thickness of 50nm. The detail image analysis of membrane thickness is given in Supplementary material.

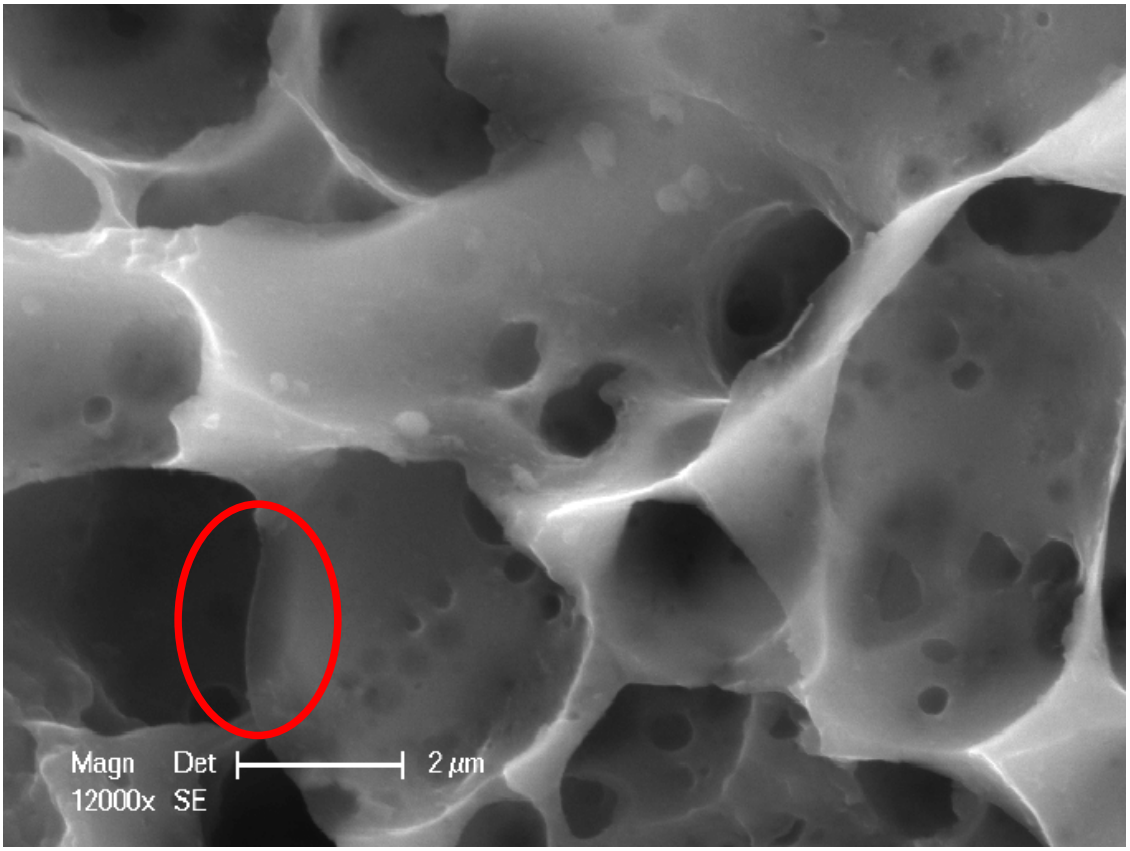

Fig. 4. Membrane structure of the porous zone showing the onset of void genesis at the walls adding additional porosity.

To calculate the surface porosity across the cross section of the porous zone and the pore size distribution, the Fig.2 is used for further image analysis (see Supplementary material for more details). Using the grey value of each pixel, a porosity rate of 66% x was found. This value does not include the 3D porosity since this is a calculated surface ratio. However, it indicates the typical porosity rate that can be achieved by a hierarchical porous structure produced by HSI.

The pixels of Fig. 2 are also analyzed to assess pores size and distribution. The pore size given by the area is converted into an equivalent diameter. Their distribution is analyzed for the whole image and plotted in Fig. 5a. The results show that the porous structure contains 60% of pores lower than 2µm in diameter. Less than 8% of the pores are greater than 5µm in diameter. Analysis of the fine pores is also performed on the original image (Fig. 2), but the selection of suitable grey range becomes tricky due to the hierarchical template of the pores and the variance of grey they exhibit. That is, the hierarchical pores have grey values close to each other, so that they can be easily merged during the segmentation operation. For the greyscale of the pores, the range of 175-255 best matches with the zone of fine pore and then enables the identification of the fine porosity (Fig. 10) (see Supplementary material for more detail). There are some hierarchical pores also counted in this analysis and they correspond to large pores correspond to a very small proportion as shown in Fig. 10. So, those hierarchical pores do not adversely affect the distribution results of the fine pores. The pores size less than 2µm represents more than 80% over the whole size range, and at least 38% of them are sub-micron size pores.

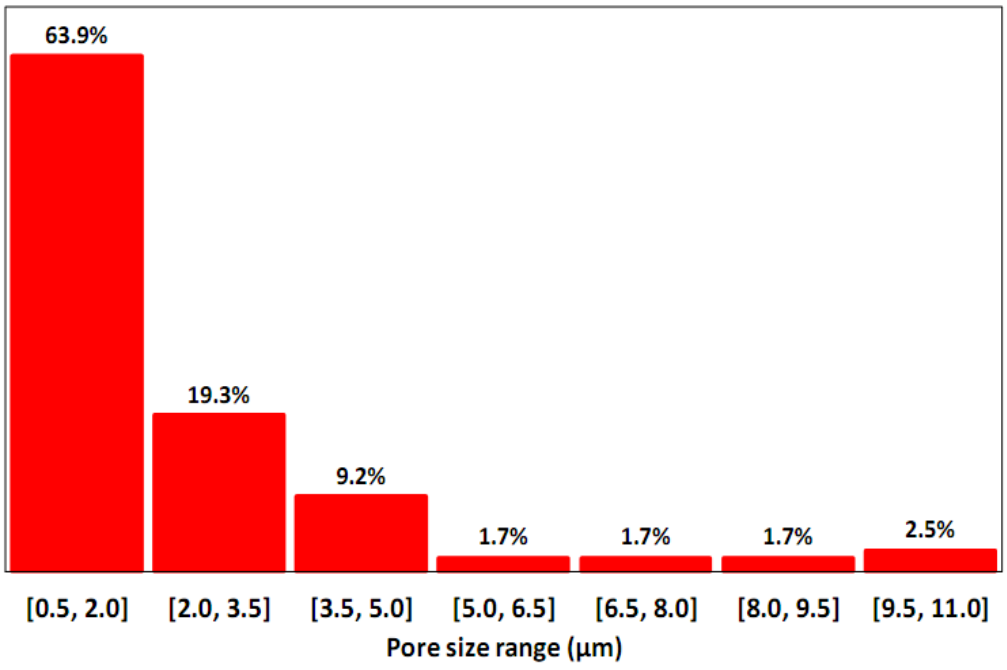

(a)

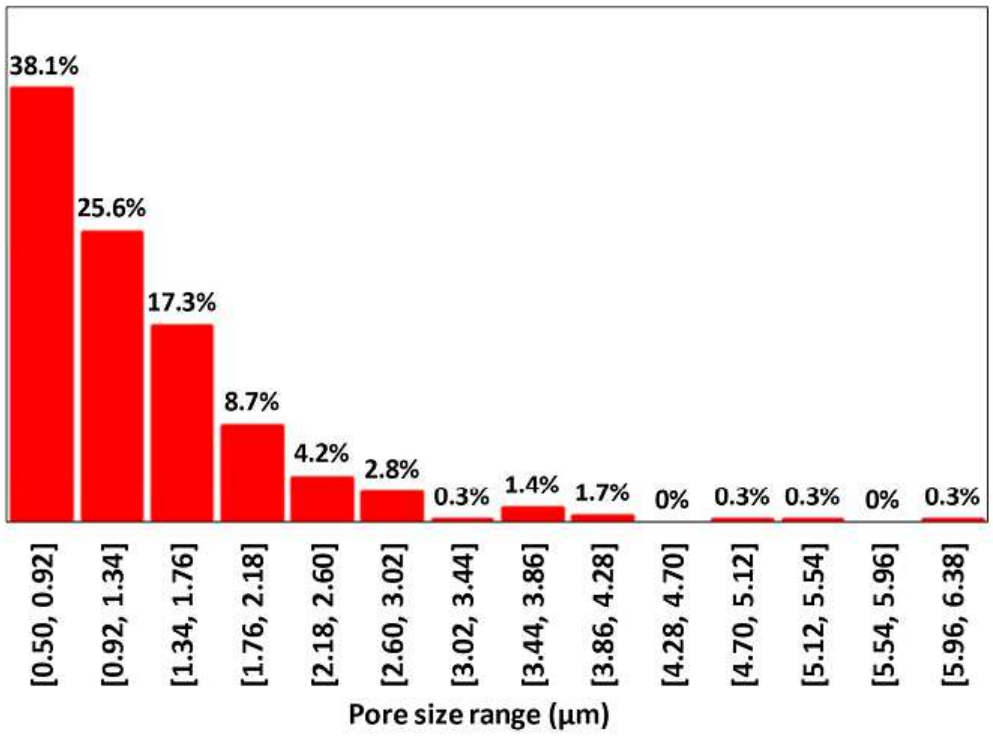

(b)

Fig. 5. Global pore sizes range and distribution calculated from the surfaces of segmented regions (a) and (b) pore size and distribution of the fine pores.

In summary, these dimensional characterizations reveal that the hierarchical porous architecture has high porosity, membrane structure including ultra-thin wall, and micron sized porosity including a significant proportion of sub-micron pores. The whole features of this porous template represent new findings that could be said unconventional with respect to the current variance of porous architectures as reported in Fig.1. In terms of the overall morphology, significant differences have been evidenced between this porous structure and those reported in Fig.1. The mechanisms that develop this new type of porous media is unusual compared to current conventional manufacturing processes. Therefore, the next section focuses on understanding the novelty of the solid interface turns into such porous template. We focus on phenomenological aspects of this transformation while they are supported by the experimental observations and computational simulation.

4. Formation of the porous cell made of porous membrane

The porous zone arises from the high-speed collision at the interface between two aluminum parts. The interface experiences rapid changes in a confined narrow zone and they are difficult to investigate using in-situ experimental observations. To identify the phenomena that prevail during the collision, we highly depend on the characteristic features of the interface generated during the process. Thus, a thermomechanical finite element computation is used in this study to further understand the governing mechanisms during the formation and development of the porous structure. Fig. 6 shows an optical microscopy observation of the porous zone at the interface, bounded between two aluminum parts. The grain boundaries of the parent material (AA6061 -T6) are visible outside the porous interface zone, that evidences thereby a formation of a new feature at the welded interface; we refer it as an intermediate zone (IZ) in this work.

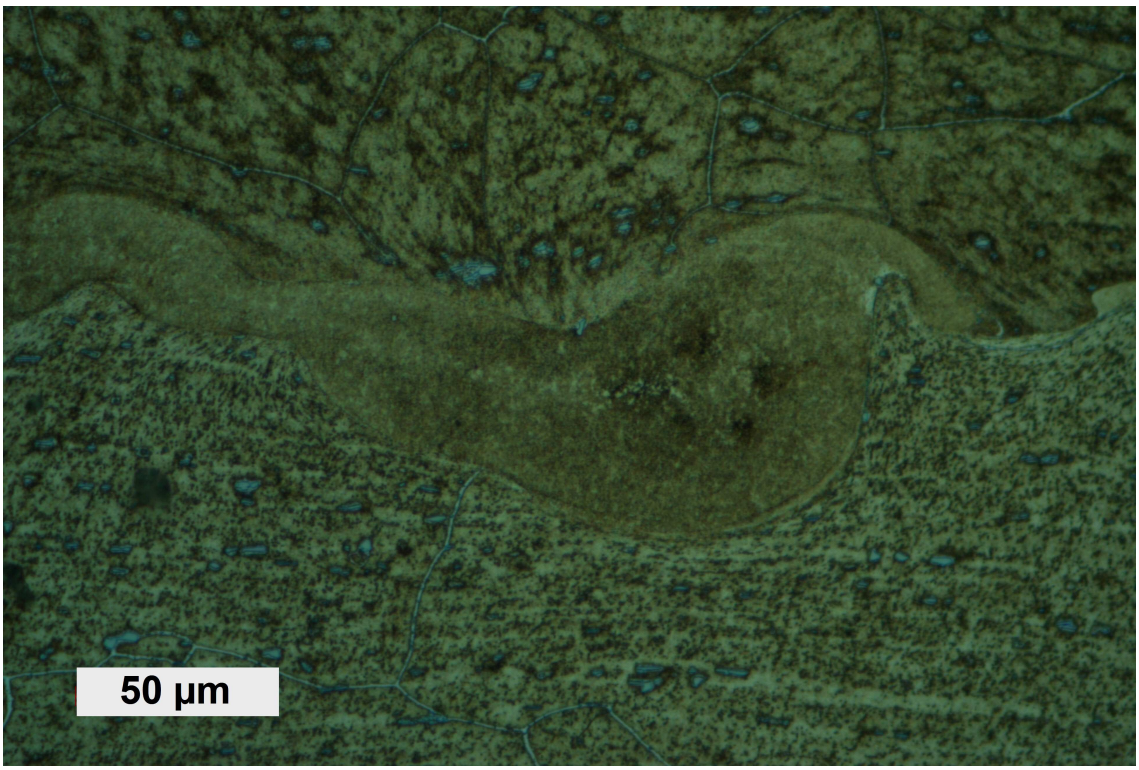

Fig. 6. Interface containing an intermediate zone (IZ) where the formation of pores occurs.

The progression of the impact between the two parts of the weld involves strong shearing at high strain rate. Several macroscopic examinations evidence shear instability phenomena such as wave formation, wake and vortex formation and jetting and emission of particles from the interface [19,22–24]. It was also observed that the grains adjacent to the bonded interface are highly elongated and flattened to form a shear affected zone (SAZ), at the vicinity of the interface [19,23]. The plastic deformation and the associated impact phenomena at the interface is significantly high to generate excessive heating of the SAZ beyond the melting point of the parent material. Virtual computations of the collision for Al/Al welding indicate that the local plastic strain reaches up to 600% and temperatures of above the melting point of aluminum within the narrow zone at the interface [22,23]. Since the zone outside of the SAZ is very large and remains cold during the high strain rate collision, the melted zone is subjected to a rapid solidification with very high cooling rate that prevents the generation of new grain boundaries by equilibrium grain growth. Thus, non-equilibrium transformations rather prevail in such solidification condition. TEM observation in an IZ across the interface was successfully realized as shown in Fig. 12a. The interaction of the electron beam with the IZ zone at position 1 (Fig. 12a) does not reveals neither periodical spots nor reflections organized into clear rings (Fig. 12b). Instead, the diffraction pattern consists of random-like structure (Fig. 12b), imputes the rapid solidification that rather freezes the atoms in their random position. Thereby, the IZ is likely to be free of grain boundaries (amorphous) or contain nanograin structures or a combination of both due to the presence of following three major phenomena, viz. high strain rate localized shearing, confined melting and fast cooling.

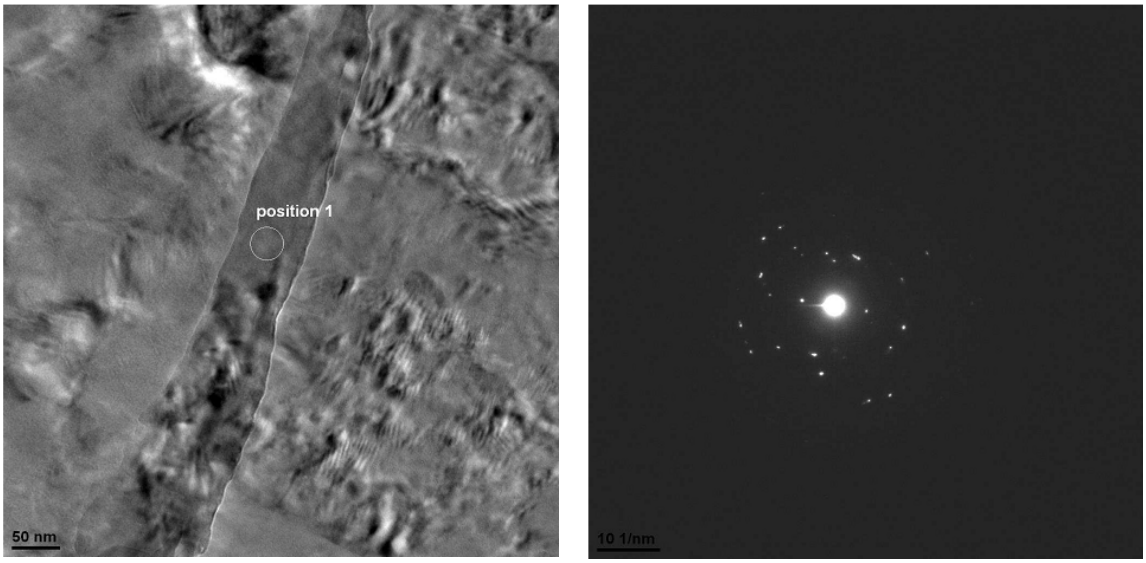

(a) (b)

Fig. 7. TEM observation revealing the IZ (a) and electron diffraction pattern corresponding to the position 1 (marked in Fig. 7a) showing random-like structure (b).

SEM observations are further used to analysis the resulting microstructure of the IZ. It shows a development of fine structure that consists of random epitaxial and columnar cells (Fig. 8a). A few dispersed black spots that emerge from this solidified zone indicates that the IZ is the favorable site for the porous structure formation. The onset of nucleation of new columnar is noticed from these random black spots that could be related to different thermal kinetics at those local regions. Fig. 8b shows a relatively more developed nucleation characterized by more submicron size pores whose shapes are nearly spherical. Observation over a larger zone provides further convincing results (Fig. 8c). The pores clearly arise from the IZ and the random aspect of the nucleation sites as well as the porosity development is still observed. Nucleation, coalescence and onset of growth into micron pores are evidenced. Moreover, the grain like structures in Fig. 8a-c confirm that they are submicron grains. Fig 8b and c also shows some zone without the absence of the grain like features that could partly being amorphous. Therefore, the complex grain structure with the combination of rapid cooling may resulted from the extremely high cooling rate and this result also support the TEM observation (Fig. 7b).

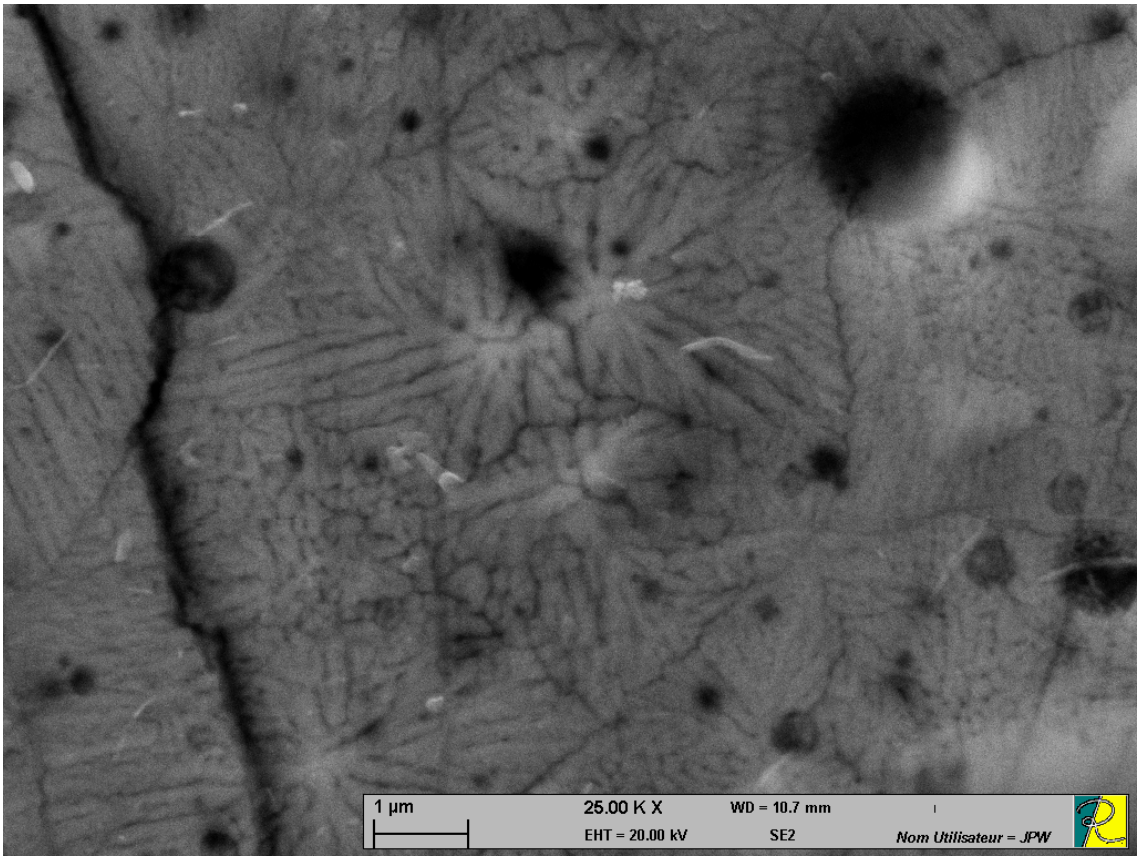

(a)

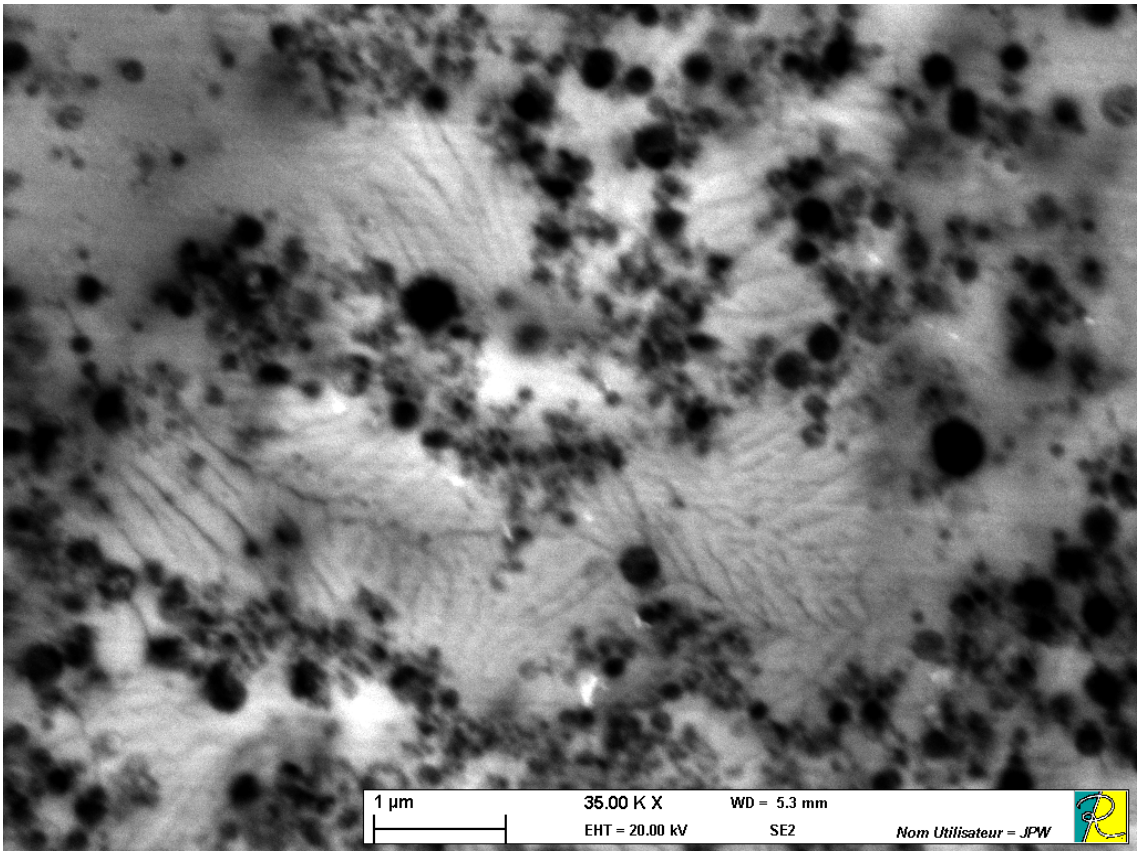

(b)

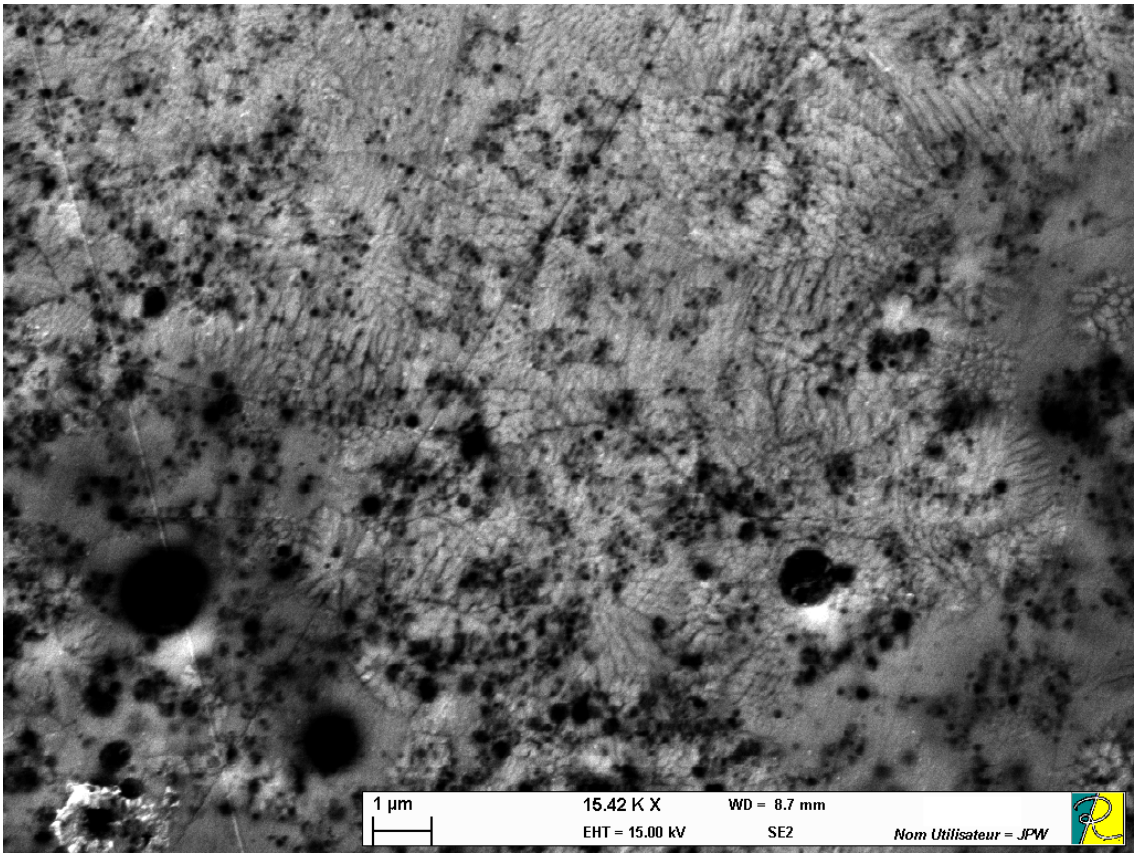

(c)

Fig. 8. SEM observation showing the nucleation of pores within the IZ revealing traces of cooling (random epitaxial and columnar cells) in (a), developed nucleation and growth onset characterized by more submicron pores with nearly spherical shape in (b), and typical heterogenous aspect of the pore formation: heterogeneous nucleation, growth and coalescence into micron pores in (c).

The evolution of the confined melting towards the porous structure is an ultra-transient phenomenon which is difficult to include among equilibrium transformations. This is a new phenomenon that has not received attention in the literature of high-speed impact welding which rather gives interest to process development and control. The mechanism that forms such fine pores at extraordinary reaction speed can be explained by an approach based on thermodynamics of phases change describing the transitions between solid, liquid and gas governed by the changes in pressure and temperature. This thermodynamic notion is more appropriate to identify the ultrafast pores formation from a phenomenological point of view.

A sublimation, i.e. a physical change directly from solid phase into gaseous phase, producing a porous media is unlikely to happen since such change is a sub-atmospheric phenomenon. Sublimation of aluminum alloy was investigated in some research studies that indicate the sublimation of Al requires very low pressures, in the range of some Pa [25,26]. Such pressures limits are excessively exceeded at the interfacial zone during MPW. The collision is extremely intense to produce impact pressures of some GPa, so the sublimation under low pressure conditions such as a condition suitable for anhydrous aluminum compounds does not prevail. Instead, a phase change from liquid state into gaseous state is more plausible. Vaporization can also be suggested but there are some aspects which make this consideration unsuitable. That is, the IZ contains more than 80% of Al content according to EDS analysis (see Supplementary material for EDS spectrum) performed during TEM observations (Table 1). Other chemical elements of at the IZ are also very weak. Moreover, the increase in temperature beyond aluminum vaporization (~2450°C) combined with the high thermal conductivity of aluminum would have produced a large melted zone instead of a confinement of heat affected zone over a very narrow distance of some micrometers (Fig 11). Therefore, assuming a vaporization of the Al is not appropriate to explain a selective nucleation of pores during HSI. The porosity obtained in the previous experimental observations exhibit heterogenous formation of pores in terms of both size and spatial distribution. A selective vaporization, conducive to such nucleation, is inconsistent with the presence of high thermal conductivity of Al which rather involves heat dissipation instead of local heat confinement. This phenomenological incompatibility between high thermal conductivity and strong confined thermal gradient that generates multiple heat spots precludes the phenomenology based on vaporization for producing the porous structure. Furthermore, the spherical nature of the pores, fine or large, and the hierarchical porosity within membrane template (Fig. 4) suggest a radial growth of pores. A porous coalescence by vaporization should therefore involve occurrence of several sites of strong radial thermal gradients enable for a progressive radial vaporization. However, such phenomenological condition is also physically unrealistic due to the high thermal conductivity of the Al.

Table 1. Chemical composition of the Al6061 material measured by EDS using TEM

Weight (%)	Chemical elements					
	C	O	Si	Cu	Mg	Al

Measurement 1	16.07	10.10	0.48	9.65	-	63.70
Measurement 2	-	8.22	-	10.97	-	80.81
Measurement 3	3.61	6.13	-	8.33	1.39	80.54
Measurement 4	8.61	5.19	-	7.91	0.75	77.53
Average	7.07	7.41	0.12	9.22	0.54	75.65

Instead of an isobaric vaporization, an isothermal transition from intermediate liquid state can explain the formation of porous structure. Following the interfacial melting, nucleation of pores appears in the Al liquid due to a fast change of pressure during the collapse of the high pressure resulting from the collision. We can suggest that the local pressure decreases below the saturated vapor pressure of the Al liquid to generate spherical vapor bubbles. Then, there is a phase change by cavitation phenomenon due to the pressure decrease, and the subsequent micron-sized bubbles create the porous structure during a rapid solidification. The pressure and temperature changes during the high strain rate collision can be characterized by a thermomechanical simulation of the collision. Thus, we can rely on a robust Eulerian method capable for computing interfacial kinetics and governing mechanisms under the influence of high strain rate impact conditions. This method allows to reproduce the interfacial characteristic changes during impact welding [22,23,26]. Fig. 9 presents typical characteristic variations of pressure and temperature obtained from Eulerian simulation of HSI. The time-dependent temperature profile at the interface evidences a strong transient peak that far exceeds the melting temperature of Al, due to an ultrafast heating induced by the excessive shear deformation at high strain rate. The melting stage lasts about 150ns that includes the increase of temperature from the melting point of Al to the maximum temperature (~1200°C) and then the drop of temperature before or during the solidification. During this very short melting-solidification stage, the local pressure varies simultaneously with a similar trend to the temperature curve. After a rapid increase of local pressure, there is a sudden decrease of pressure with a rate of about 100MPa/ns that creates the depressurization condition necessary for cavitation. Subsequently, solidification occurs at high cooling rate of 10°C/ns that quickly freezes the cavities along with the progress of the depressurization. The continuous process of pore formation from the solid state, through the successive transitions, is described on a schematic representation of thermodynamic pressure-temperature diagram of Al (Fig. 10), which specifies the phenomenological changes during HIS and physical parameter variations during the porous structure formation.

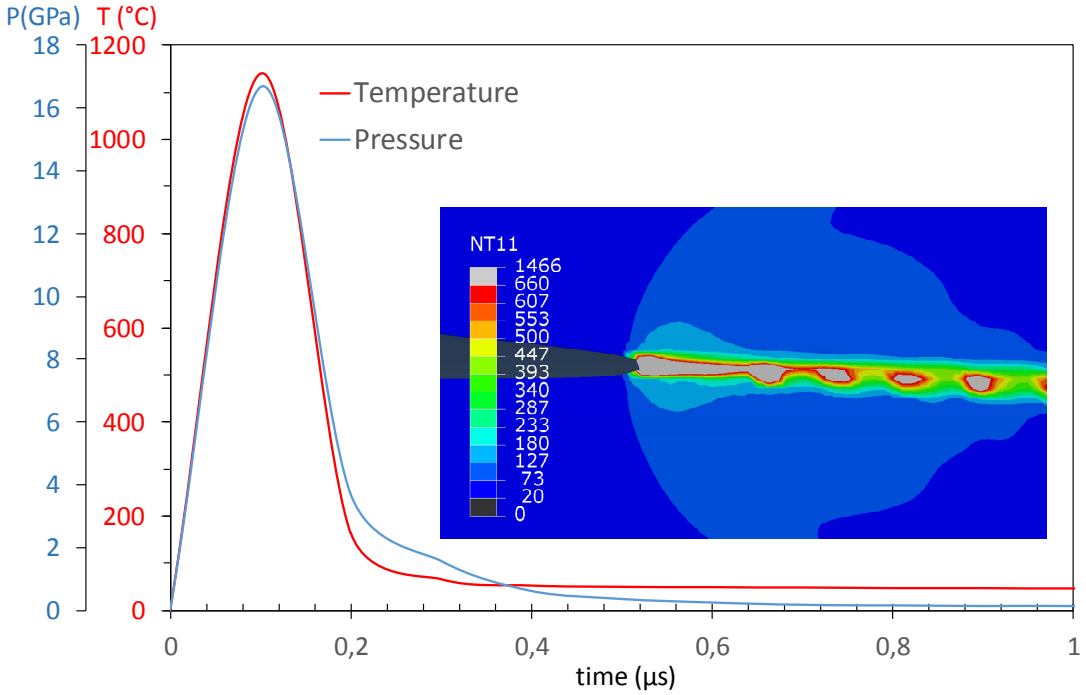

Fig. 9. Typical variation of pressure and temperature computed during the HSI using Eulerian simulation, and typical computed molten zone predicting the morphology of IZ corresponds to the porous structure formation (NT11 denotes the temperature in °C).

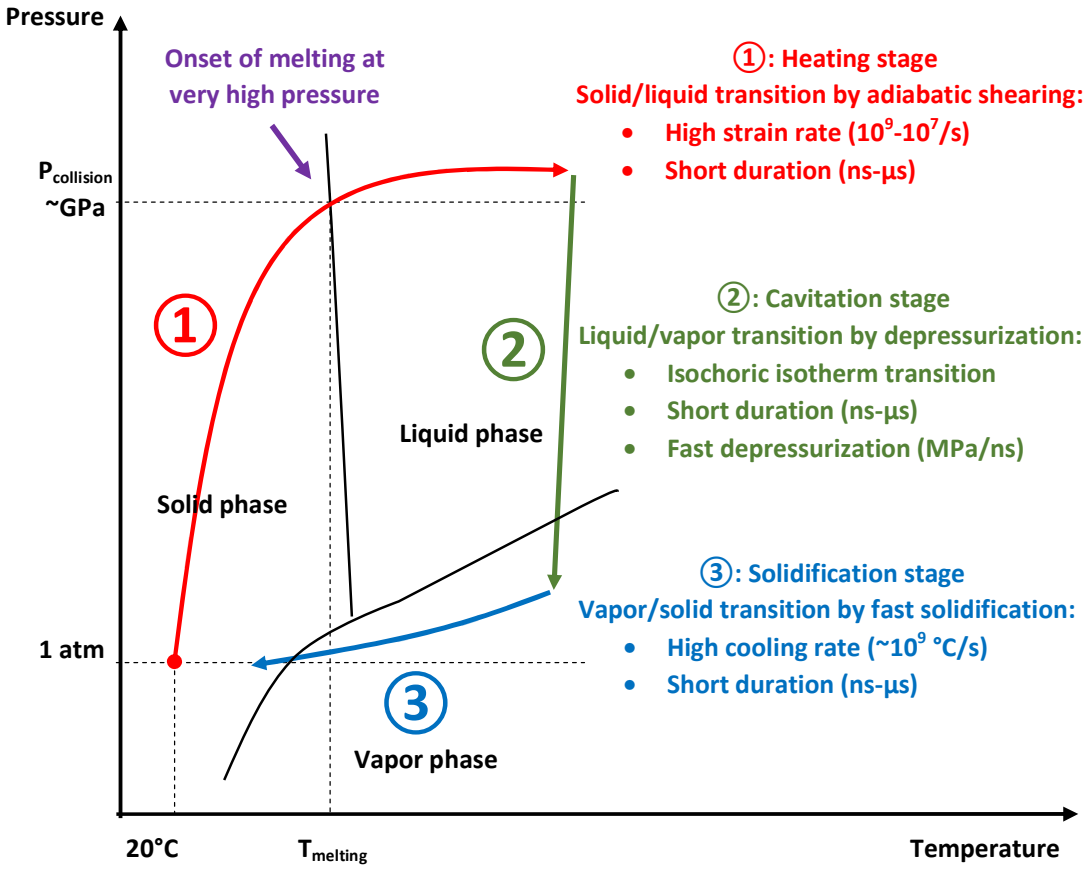

Fig. 10. Schematic illustration of thermodynamic pressure-temperature diagram explaining the successive transitions during the porous structure formation.

From a phenomenological point of view, the spherical shape of pores can be attributed to a radial growth of each micropore due to an isochoric fast expansion during the depressurization. The fluid rupture due to the surface tension within the molten zone as consequence of the depressurization explains the nucleation of cavities. New pores can also nucleate while existing pores become larger pores enabling the hierarchical porosity. This could be the potential mechanism of coalescence for the creation of the open porosity. A solidification shrinkage may also contribute to pores growth and coalescence but the likelihood of such effect and the behaviour of the solid architecture during the cooling stage must be fully understood.

The randomness of the pores size and nucleation sites can be attributed to a heterogeneity of the interfacial pressure within the irregularly shaped melted zone. Although, the variance of

pores size provides some hint for the interpretation of the resulting radial growth and coalescence of vapor bubbles, the governing mechanisms should be further understood. During MPW, these interfacial processes are extremely fast, last a few microseconds, so identifying experimentally reliable phenomena of bubbles growth and coalescence becomes tricky. However, a comparison between two experimental observations provide some considerable insight in the formation of porous structure. Two MPW tests were conducted using similar colliding workpieces (similar flyer) but under different collision conditions. The porous structure shown in Fig. 11a and b are obtained for the initial air gap (prior to the collision test) of g = 1.5mm with the discharge voltage of U = 6.5kV, and initial air gap of g = 5mm with the discharge voltage of U = 7.5kV, respectively. The intensity of the collision makes the major difference between these two cases. Higher discharge voltage and higher initial gap is conducive to higher impact velocity and resulting with higher collision pressure, higher strain rate, large plastic straining and significantly more heating. Characterization of welded interfaces clearly reveals the consequences of the collision conditions that becomes important with the increase in air gap and discharge voltages [17–19]. Regarding the porous structure formation, the parameter set with g = 1.5mm and U = 6.5kV rather creates a dense structure (Fig. 11a) compared to the porous structure obtained with g = 5mm and U = 7.5kV which provides significantly developed pores, i.e. with larger and hierarchical pores, but also membrane architecture (Fig. 11b). The difference of cavitation between these two cases can be attributed to a difference of depressurization. The more intense collision provides the stronger impact pressure, therefore later (g=5mm, U=7.5kV) experiences the higher depressurization gap and increased fluid rupture due to higher inherent fluid tension. At low collision intensity (g=1.5mm, U=6.5kV), the depressurization reaches the conditions to begin the cavitation process while a weak growth and onset of coalescence occur (Fig. 11a). The strong collision (g=5mm, U=7.5kV) provides significantly high depressurization which enables a powerful coalescence that forms the highly porous structure (Fig. 11b) during solidification at high cooling rate.

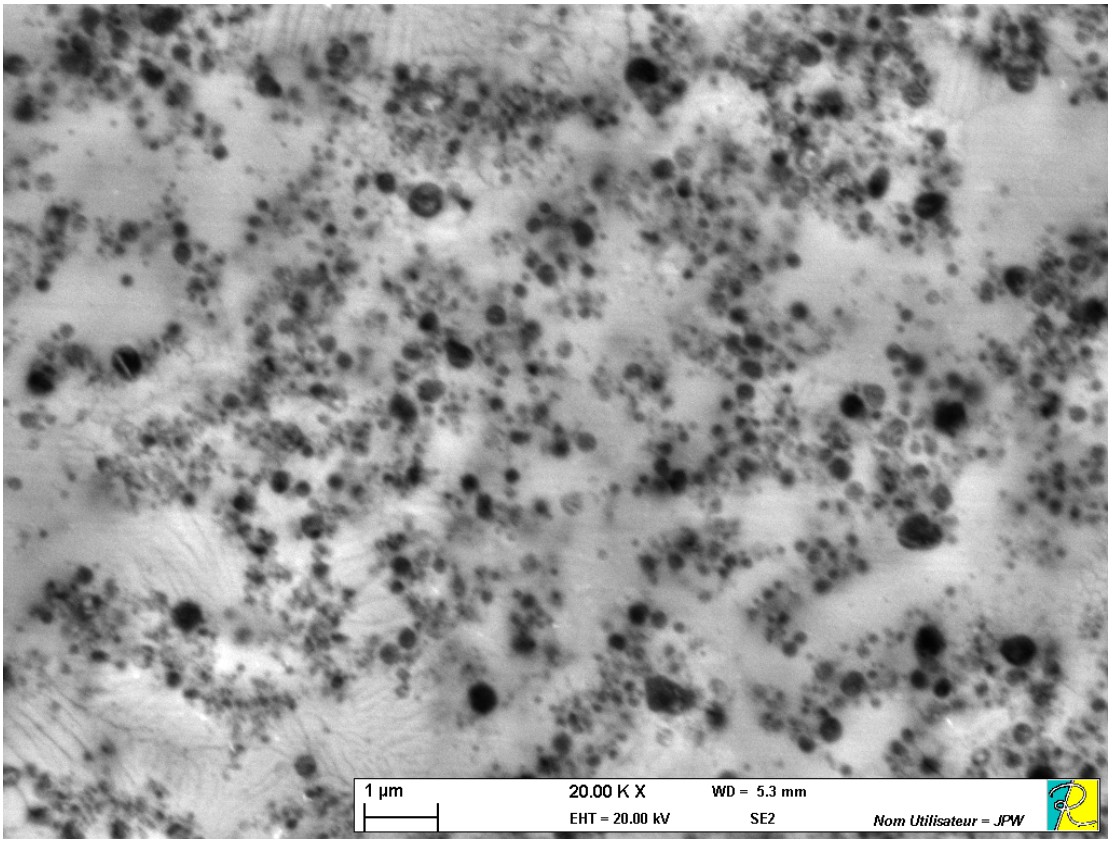

(a)

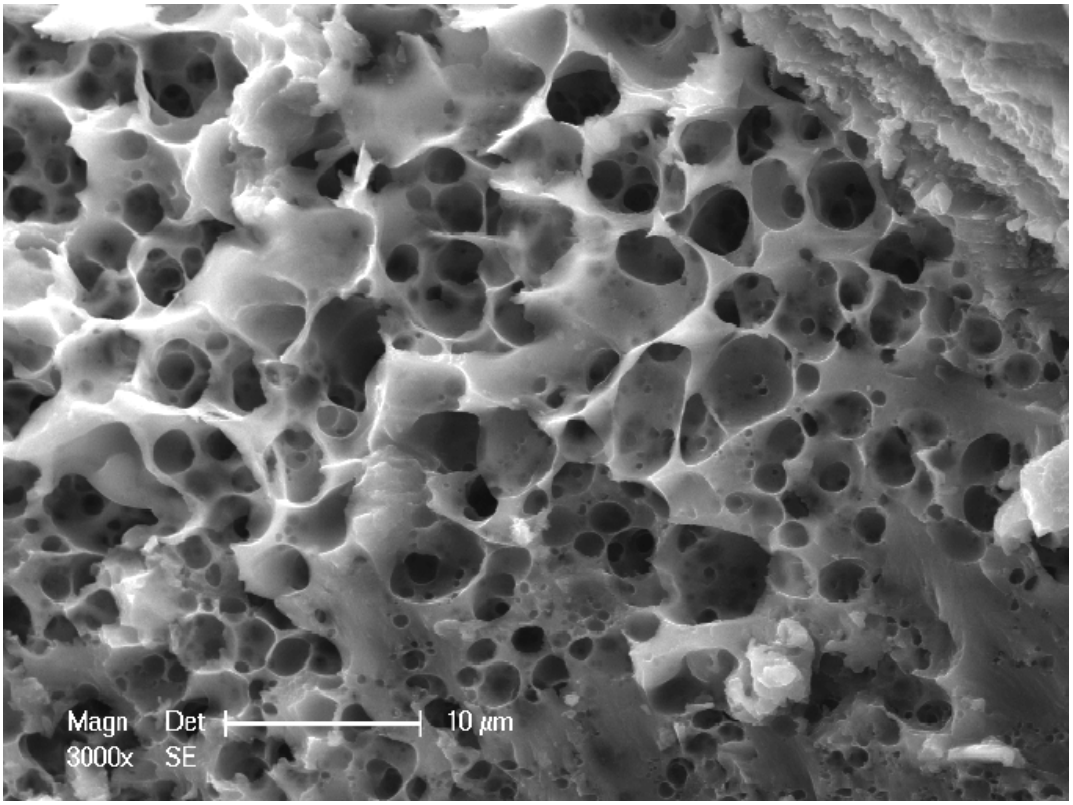

(b)

Fig. 11. Difference of cavitation attributed to difference in depressurization. Weak cavitation attributed to a low collision intensity with g = 1.5mm and U = 6.5 kV in (a), and highly developed porous structure attributed to higher impact pressure obtained with g = 5mm and U = 7.5kV in (b).

5. Conclusions

A new type of porous architecture is produced by high speed collision exhibiting an unusual feature of a porous template that consists of a hierarchical porosity made of nearly spherical pores. Dimensional analysis reveals that the porous structure has high porosity of 66% in the cross-section area, membrane structure including ultra-thin wall of 50 nm, and micron sized porosity including a significant proportion of sub-micron pores. The pores appear within a solidified structure where random nucleation of cavities occur. The spherical shape and the

hierarchical organization of the porosity suggest a mechanism during the development of pores due to a cavitation phenomenon. Based on the thermodynamic considerations combined with computational simulation of the high strain rate collision, pores nucleation, growth and coalescence are explained as an ultra-fast isothermal and isochoric transition of a molten phase into a vapor phase. During these phenomena, cavities emerge due to a high rate of depressurization followed by a solidification at rapid cooling rate to produce the porous structure. An experimental comparison between cavitation onset and a fully developed cavitation allows to corelate the degree of cavitation with the depressurization intensity. The highly developed porous structure is favoured by the conditions corresponding to strong collision, i.e. high impact pressure followed by a significant depressurization. Together, those fast-dynamic phenomena represent a potential method for the manufacturing porous structures based on a micro-cavitation mechanism. This new finding merits to be further explored in the future.

Acknowledgments

Authors acknowledge the “Région Picardie” and “Le fonds européen de développement économique et régional (FEDER)” for funding of the MSIM project (2010/2012) and COILTIM project (2014/2020). Jishuai Li acknowledges the financial support of China Scholarship Council (CSC) during his PhD candidature at Université de Technologie de Compiègne.

Appendix A: Supplementary material

Supplementary material associated with this article can be found, in the online version, at **« Please note, that the corresponding DOI link will be specified here later during the production».**

References

[1] W. Wang, R. Burgueño, J.-W. Hong, I. Lee, Nano-deposition on 3-D open-cell aluminum foam materials for improved energy absorption capacity, Mater. Sci. Eng. A. 572 (2013) 75–82. doi:10.1016/j.msea.2013.02.032.

[2] S.-Q. Fan, C.-J. Li, C.-X. Li, G.-J. Liu, G.-J. Yang, L.-Z. Zhang, Preliminary Study of Performance of Dye-Sensitized Solar Cell of Nano-TiO2 Coating Deposited by Vacuum Cold Spraying, Mater. Trans. JIM. 47 (2006) 1703–1709. doi:10.2320/matertrans.47.1703.
[3] Y. Luan, Y.-W. Xue, Z.-G. Shi, Synthesis of hierarchically macro/meso/microporous carbon spheres and its application in fast rechargeable electric double layer capacitor, Mater. Lett. 88 (2012) 30–32. doi:10.1016/j.matlet.2012.08.046.
[4] L.-P. Lefebvre, J. Banhart, D.C. Dunand, Porous Metals and Metallic Foams: Current Status and Recent Developments, Adv. Eng. Mater. 10 (2008) 775–787. doi:10.1002/adem.200800241.
[5] K. Xia, Q. Gao, J. Jiang, H. Wang, An unusual method to prepare a highly microporous carbon for hydrogen storage application, Mater. Lett. 100 (2013) 227–229. doi:10.1016/j.matlet.2013.03.026.
[6] G. Ryan, A. Pandit, D.P. Apatsidis, Fabrication methods of porous metals for use in orthopaedic applications, Biomaterials. 27 (2006) 2651–2670. doi:10.1016/j.biomaterials.2005.12.002.
[7] C. Zhang, J. Sun, J. Xu, X. Wang, H. Ji, C. Zhao, Z. Zhang, Formation and microstructure of nanoporous silver by dealloying rapidly solidified Zn–Ag alloys, Electrochimica Acta. 63 (2012) 302–311. doi:10.1016/j.electacta.2011.12.103.
[8] Y. Li, Y.-Y. Song, C. Yang, X.-H. Xia, Hydrogen bubble dynamic template synthesis of porous gold for nonenzymatic electrochemical detection of glucose, Electrochem. Commun. 9 (2007) 981–988. doi:10.1016/j.elecom.2006.11.035.
[9] S. Cherevko, C.-H. Chung, Direct electrodeposition of nanoporous gold with controlled multimodal pore size distribution, Electrochem. Commun. 13 (2011) 16–19. doi:10.1016/j.elecom.2010.11.001.
[10] H. Kaiser, Selective dissolution of high and low diffusivity alloys—A comparison of kinetical and micromorphological aspects, Corros. Sci. 34 (1993) 683–699. doi:10.1016/0010-938X(93)90280-T.
[11] M.E. Cox, D.C. Dunand, Bulk gold with hierarchical macro-, micro- and nano-porosity, Mater. Sci. Eng. A. 528 (2011) 2401–2406. doi:10.1016/j.msea.2010.11.072.
[12] V. Loryuenyong, A. Buasri, C. Srilachai, H. Srimuang, The synthesis of microporous and mesoporous titania with high specific surface area using sol–gel method and activated carbon templates, Mater. Lett. 87 (2012) 47–50. doi:10.1016/j.matlet.2012.07.090.
[13] W. Xing, S.-P. Zhuo, X. Gao, Preparation of hierarchical porous carbon by post activation, Mater. Lett. 63 (2009) 1311–1313. doi:10.1016/j.matlet.2009.03.008.
[14] S.P. Murzin, Exposure to laser radiation for creation of metal materials nanoporous structures, Opt. Laser Technol. 48 (2013) 509–512. doi:10.1016/j.optlastec.2012.11.031.
[15] B. Chen, G.-J. Yang, C.-J. Li, C.-X. Li, Preparation of hierarchical porous metallic materials via deposition of microporous particles, Mater. Lett. 176 (2016) 237–240. doi:10.1016/j.matlet.2016.04.083.
[16] R.N. Raoelison, D. Racine, Z. Zhang, N. Buiron, D. Marceau, M. Rachik, Magnetic pulse welding: Interface of Al/Cu joint and investigation of intermetallic formation effect on the weld features, J. Manuf. Process. 16 (2014) 427–434. doi:10.1016/j.jmapro.2014.05.002.
[17] R.N. Raoelison, N. Buiron, M. Rachik, D. Haye, G. Franz, Efficient welding conditions in magnetic pulse welding process, J. Manuf. Process. 14 (2012) 372–377. doi:10.1016/j.jmapro.2012.04.001.
[18] R.N. Raoelison, N. Buiron, M. Rachik, D. Haye, G. Franz, M. Habak, Study of the elaboration of a practical weldability window in magnetic pulse welding, J. Mater. Process. Technol. 213 (2013) 1348–1354. doi:10.1016/j.jmatprotec.2013.03.004.
[19] R.N. Raoelison, T. Sapanathan, N. Buiron, M. Rachik, Magnetic pulse welding of Al/Al and Al/Cu metal pairs: Consequences of the dissimilar combination on the interfacial behavior during the welding process, J. Manuf. Process. 20, Part 1 (2015) 112–127. doi:10.1016/j.jmapro.2015.09.003.

[20] N. de Jonge, F.M. Ross, Electron microscopy of specimens in liquid, Nat. Nanotechnol. 6 (2011) 695–704. doi:10.1038/nnano.2011.161.
[21] J.D. Stoll, A. Kolmakov, Electron transparent graphene windows for environmental scanning electron microscopy in liquids and dense gases, Nanotechnology. 23 (2012) 505704. doi:10.1088/0957-4484/23/50/505704.
[22] R.N. Raoelison, T. Sapanathan, E. Padayodi, N. Buiron, M. Rachik, Interfacial kinematics and governing mechanisms under the influence of high strain rate impact conditions: Numerical computations of experimental observations, J. Mech. Phys. Solids. 96 (2016) 147–161. doi:10.1016/j.jmps.2016.07.014.
[23] T. Sapanathan, R.N. Raoelison, E. Padayodi, N. Buiron, M. Rachik, Depiction of interfacial characteristic changes during impact welding using computational methods: Comparison between Arbitrary Lagrangian - Eulerian and Eulerian simulations, Mater. Des. 102 (2016) 303–312. doi:10.1016/j.matdes.2016.04.025.
[24] T. Sapanathan, R.N. Raoelison, N. Buiron, M. Rachik, Magnetic Pulse Welding: An Innovative Joining Technology for Similar and Dissimilar Metal Pairs, in: M. Ishak (Ed.), Join. Technol., InTech, 2016. http://www.intechopen.com/books/joining-technologies/magnetic-pulse-welding-an-innovative-joining-technology-for-similar-and-dissimilar-metal-pairs (accessed October 7, 2016).
[25] Vacuum Sublimation of Anhydrous Aluminum Chloride--《Chinese Journal of Vacuum Science and Technology》2009年03期, (n.d.). http://en.cnki.com.cn/Article_en/CJFDTOTAL-ZKKX200903025.htm (accessed September 24, 2018).
[26] R. Teghil, D. Ferro, L. Bencivenni, M. Pelino, A thermodynamic study of the sublimation processes of aluminium and copper acetylacetonates, Thermochim. Acta. 44 (1981) 213–222. doi:10.1016/0040-6031(81)80042-1.

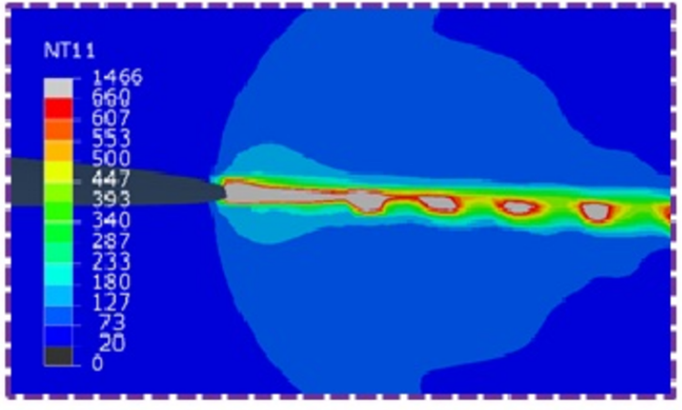
NT11
1466
660
607
553
500
447
393
340
287
233
180
127
73
20
0

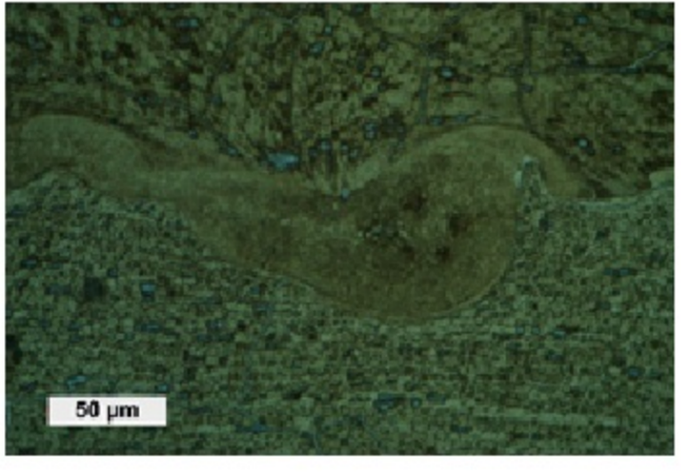
50 µm

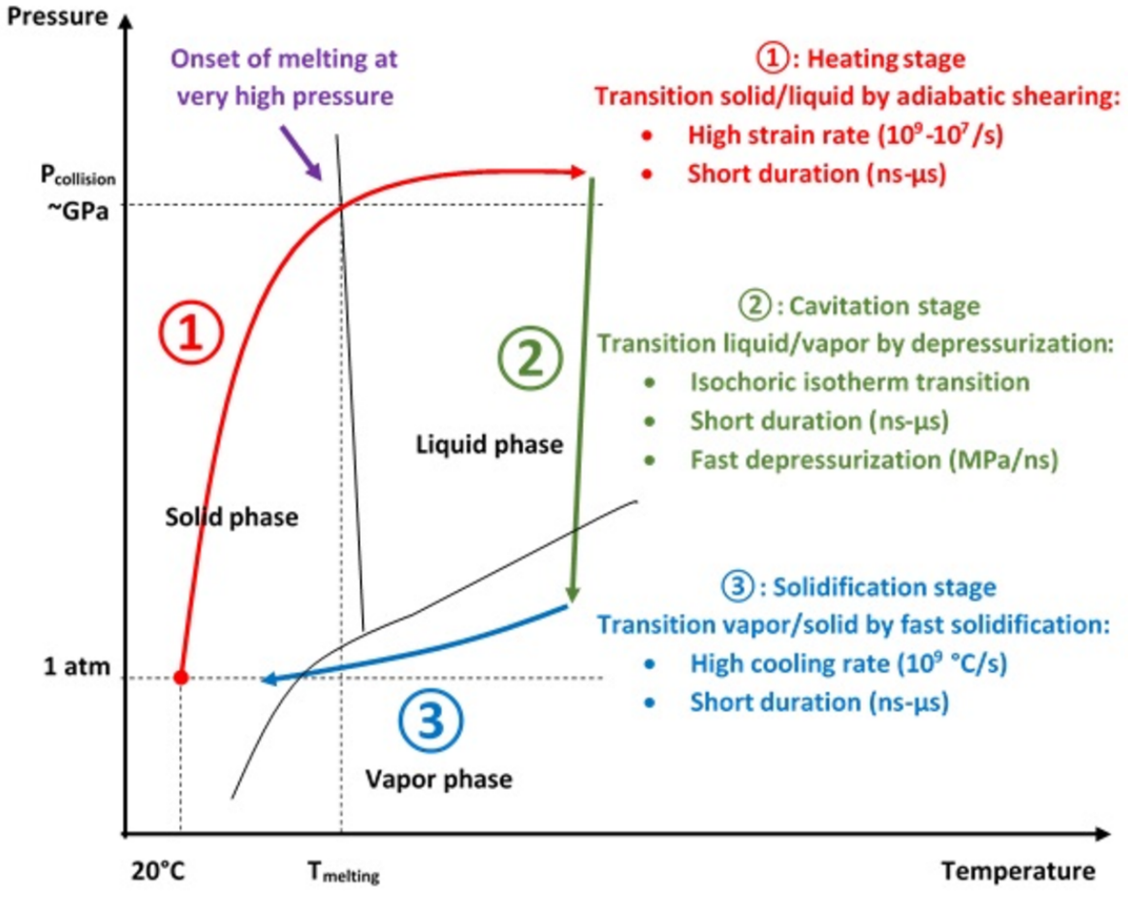
Pressure
Onset of melting at very high pressure
$P_{collision}$ ~GPa
1 atm
1
2
3
Solid phase
Liquid phase
Vapor phase
20°C
$T_{melting}$
Temperature
①: Heating stage
Transition solid/liquid by adiabatic shearing:
• High strain rate (10^9-10^7/s)
• Short duration (ns-µs)
②: Cavitation stage
Transition liquid/vapor by depressurization:
• Isochoric isotherm transition
• Short duration (ns-µs)
• Fast depressurization (MPa/ns)
③: Solidification stage
Transition vapor/solid by fast solidification:
• High cooling rate (10^9 °C/s)
• Short duration (ns-µs)

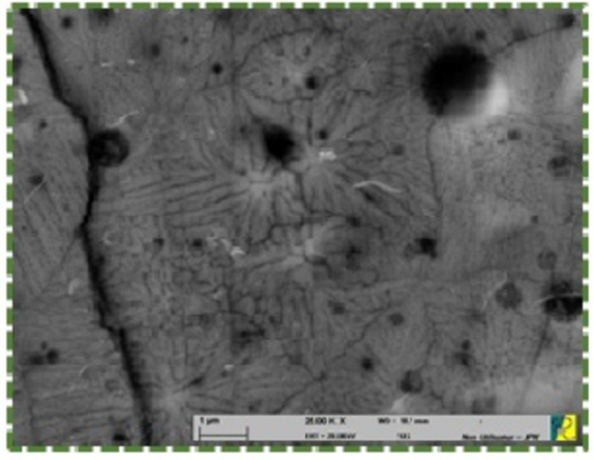

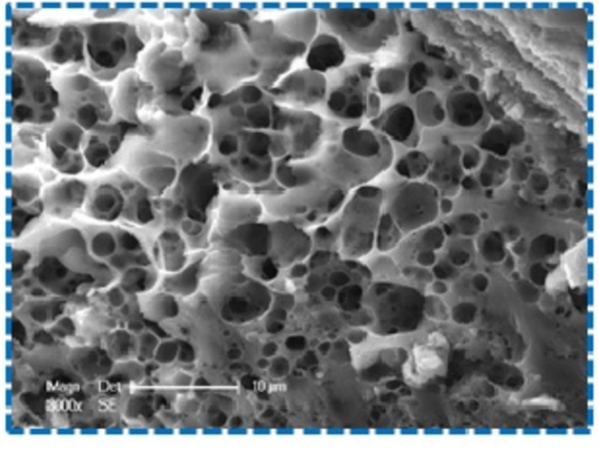
10 µm